Fermilab Library
0 1160 0054383 9
STEWARD-1234
9
FERMILAB
DEC 1? 199
LIBRARY

PREPRINTS of the STEWARD OBSERVATORY

THE UNIVERSITY OF ARIZONA
TUCSON, ARIZONA 85721 U.S.A.

No. 1234

THE LARGE SIZE OF LYMAN ALPHA GAS CLOUDS AT INTERMEDIATE REDSHIFTS*

Nadine Dinshaw†, Craig B. Foltz‡, Chris D. Impey†, Ray J. Weymann*, and Simon L. Morris‖

*Based on observations with the NASA/ESA Hubble Space Telescope, obtained at the Space Telescope Science Institute, which is operated by the Association of Universities for Research in Astronomy, Inc., under NASA contract NAS5-26555.

†Steward Observatory, University of Arizona, Tucson, Arizona 85721, U.S.A.
‡Multiple Mirror Telescope Observatory, University of Arizona, Tucson, Arizona 85721, U.S.A.
*Carnegie Observatories, 813 Santa Barbara Street, Pasadena, California 91101-1292, U.S.A.
‖Dominion Astrophysical Observatory, 5071 West Saanich Road, Victoria, B.C. V8X 4M6, Canada
Victoria
Carnegie Inst. Observatories J

To Appear in Nature.

The large size of Lyman alpha gas clouds at intermediate redshifts*

Nadine Dinshaw[†], Craig B. Foltz[‡], Chris D. Impey[†], Ray J. Weymann[*], and Simon L. Morris[||]

The absorption lines of Lyman α observed in the spectra of high redshift quasars are thought to arise in cosmologically-distributed, intervening "clouds," the origin and physical nature of which are still unknown. Various models have been proposed, including pressure-confined clouds in a hot intergalactic medium[1], relics of primordial density fluctuations associated with the cold dark matter (CDM) scenario for the biased formation of galaxies[2], gravitationally-confined clouds in CDM minihalos[3], and shocks resulting from explosive galaxy formation[4]. To distinguish between these models requires some knowledge of the cloud size and geometry. Here we present ultraviolet spectra of the Lyman α forest of the quasar pair 0107-025A,B in which we detect four absorption lines common to both spectra in the redshift range $0.5 \leq z \leq 0.9$, and six lines which are seen in the spectrum of one quasar but not the other. Assuming that these are Lyman α lines, the directly-measured lower limit on the characteristic radii of the clouds is between 160 and 180 h_{100}^{-1} kpc (where $h_{100}^{-1} \equiv H_0/100$ km s^{-1} Mpc^{-1}, $q_0 = 0.5$). The typical velocity difference between the common absorption lines along the two lines of sight is only about 100 km s^{-1}. These direct measurements lead to a picture of absorbing clouds that are both larger in extent and more quiescent than can easily be explained by current theoretical models.

The close pair of quasars, 0107-025A,B ($z_{em} = 0.956, 0.952$; angular separation 1.44′), were observed on 1994 February 12 with the Faint Object Spectrograph (FOS) on the reburbished *Hubble Space Telescope* (*HST*). The G190H grating was used on the red side of the FOS with the 1″ circular aperture. The reciprocal dispersion of the G190H is 0.3 Å pixel^{-1}, corresponding to a spectral resolution (FWHM) of 1.4 Å, or about 200 km s^{-1}. A total of 222 minutes integration time was accumulated on A and 108 minutes on B covering the wavelength range 1625–2300 Å. Fig. 1 shows the flux calibrated *HST* spectra.

---

*Based on observations with the NASA/ESA Hubble Space Telescope, obtained at the Space Telescope Science Institute, which is operated by the Association of Universities for Research in Astronomy, Inc., under NASA contract NAS5-26555.

[†]Steward Observatory, University of Arizona, Tucson, Arizona, 85721 USA

[‡]Multiple Mirror Telescope Observatory, University of Arizona, Tucson, AZ 85721, USA

[*]Carnegie Observatories, 813 Santa Barbara St., Pasadena, CA 91101-1292, USA

[||]Dominion Astrophysical Observatory, 5071 W. Saanich Rd., Victoria, B.C V8X 4M6, Canada

Absorption lines were fitted by Gaussians using algorithms identical to those of the *HST QSO Absorption Line Key Project.*[5] To avoid introducing spurious absorption lines into the analysis, we considered only those lines detected at the $> 5\sigma$ confidence level, and we also restricted our sample to lines with wavelengths longward of 1800 Å, shortward of which the S/N degrades rapidly and the identification of Lyman α lines is confused by the presence of higher order Lyman lines. This procedure ensures that in the range 1800-2300Å, all lines with $W_o \geq 0.33$Å should be detected at the 5σ limit in *both* objects. In addition, since absorption line systems containing metal lines may have different properties than the Lyman α forest lines, we selected for further discussion only those lines that we believe are neither members of metal-line containing systems, higher order Lyman series lines, nor, of course, Galactic absorption lines. The lines so selected are listed in Table 1 and marked by ticks in Figure 1.

The lines listed in Table 1 are believed to be Lyman α absorption lines for the following reasons: (1) the lines are not attributable to Galactic absorption features; (2) in some cases (lines 4, 5, 6, 7 in A and 4, 6, 7 in B), there are statistically real lines attributable to higher order Lyman lines at the same redshift; (3) given the number of Lyman α forest lines per unit redshift determined from other investigations[5] we expect to see about 9 ± 3 Lyman α lines with rest equivalent width > 0.32 Å in each quasar's spectrum in the wavelength range from 1800–2300 Å, and we observe seven lines in both A and B; and (4) we have not identified any metal lines associated with the Lyman α lines, though our current wavelength coverage is not extensive enough to search for either the C IV or Mg II doublet.

Table 1 contains four pairs of lines which are seen at very similar wavelengths in each spectrum. In all cases the redshift differences between the two features comprising the pair are small, $\Delta z < 0.0009$. The probability of getting *four* or more pairs of lines out of a total sample of 14 within this redshift difference is $\sim 10^{-7}$. We interpret these as cases where the lines of sight to the two quasars pierce the same absorber, so the lower limit on the transverse *diameter* of an absorber seen along both lines of sight is simply the proper separation of the lines of sight at the redshift of the absorber. For the common pairs observed here, this separation is $320 - 360$ kpc implying that the lower limits on the transverse *radii* range from about $160h_{100}^{-1}$ kpc for the lowest redshift pair at $z = 0.536$ to more than $180h_{100}^{-1}$ kpc for the pair at $z = 0.877$ (for $q_0 = 0.5$; assuming $q_0 = 0$, these limits become 180 and $225h_{100}^{-1}$ kpc, respectively). These lower limits are independent of any assumptions about the cloud structure or geometry.

The radial velocities measured along the two lines of sight reflect differences in bulk motions (*e.g.* rotation, expansion or contraction) of the absorbing gas seen over scales equal to the separation of the lines of sight. The limit on the accuracy of these measurements is dominated by two types of errors: (1) a systematic uncertainty due to *HST* pointing errors causing the two quasar images to be placed differently within the 1″ aperture of the FOS, and (2) random uncertainties arising in the wavelength calibration and line-fitting procedures. Since the observations of the two quasars used the same guide star, the *HST* pointing error

projected along the dispersion direction is expected to introduce an uncertainty of 0.28 Å or about 42 km s^{-1}.[6] Since this effect is systematic, shifting all of the lines in one spectrum relative to those in the other, it should be manifest in the mean of the velocity differences of the common lines, which range from -146 km s^{-1} to 112 km s^{-1} (Table 1). The mean velocity difference is only 26 km s^{-1}. Furthermore, the measured shift between the wavelengths of the Galactic Al II $\lambda 1671$ line is 20 ± 36 km s^{-1}. Both of these lead us to believe that there is no large systematic shift between the two spectra. The random uncertainty in the measured radial velocity *difference* between two lines is conservatively estimated to be about 17 km s^{-1} while the rms velocity difference for the four coincident pairs is 104 km s^{-1}. Therefore, we conclude that we are seeing statistically significant, albeit small, velocity differences over scales of several hundred kpc.

In the foregoing discussion we have consistently referred to 'cloud radii' rather than 'correlation lengths'. The present observations do not allow us to directly discriminate between single coherent clouds versus correlated but distinct structures. Assuming the former and that the clouds are identical and spherical, it is possible, using standard maximum likelihood techniques[7], to estimate the most probable value as well as the upper and lower 95% confidence limits for the radius, R, of the clouds. Here, by "radius" we simply mean the impact parameter which produces column densities corresponding to our equivalent width detection limit. The probability distribution $P(R)$ [solid curve] and its cumulative distribution [dashed curve] for $q_0 = 0.5$ are plotted in Figure 2. The most probable value of R given by the peak of the solid curve is $350h_{100}^{-1}$ kpc. The 95% confidence lower and upper bounds on the cloud radius estimated from the dashed curve correspond to $270 < R < 860h_{100}^{-1}$ kpc. For $q_0 = 0.0$ the radii are larger by about 20%.

Previous constraints on Lyman α forest absorber sizes,[8–11] also based on the presence of common absorption lines in the spectra of physical or gravitationally-lensed pairs of quasars suggest cloud sizes about an order of magnitude smaller. Recent observations of the lensed pair HE 1104-1805 have been used to infer a 2σ model-dependent lower limit on the cloud radius, at redshift $z \simeq 2.5$, of $25h_{100}^{-1}$ kpc[12] and two very recent independent studies of the quasar pair 1343+2640 A,B separated by $9.5''$ suggest cloud radii of at least $\sim 20h_{100}^{-1}$ kpc at $z \simeq 2$.[13,14]

For typical Doppler widths, neutral hydrogen column densities and expected values of the ionizing radiation field at these redshifts,[15] static self-gravitating clouds are expected to be smaller than this, especially with any dark matter binding (cf ref. 16; eq 8); pressure confinement would make them smaller still. However, if the clouds are in the process of collapsing they would be larger than these simple estimates for static structures.

Alternatively, the large characteristic sizes implied by Figure 2 may be more indicative of correlation lengths than actual cloud sizes. There is evidence that luminous galaxies have effective cross sections for producing Lyman α with $W_o \geq 0.3$ Å of several hundred kpc,[17] and it has also been suggested that pressure-confined tidal debris resulting from mergers or close encounters of galaxies spread over several hundred kpc may be involved[18]. For models

such as these, the large characteristic size for the Lyman α structures which our observations establish is not especially surprising. However, the small projected velocity differences may be more difficult to understand, since clouds unaffected by drag in the disks or virialized halos of normal galaxies would have velocity dispersions of $200 - 300$ km s^{-1}.[19] Similarly, the characteristic line-of-sight velocities associated with small groups of galaxies, or with dwarf galaxies orbiting around luminous galaxies, are typcially 150 km s^{-1}.[20] We must note, however, that our observed typical velocity difference of 104 km s^{-1} is based upon only four pairs of lines and so may not be highly statistically significant.

Regardless of which, if any, of the models above may prove to be correct, our observations suggest velocity differences of less than a few hundred km s^{-1} over scales of several hundred kpc. By contrast, examination of the distribution of the small number of Lyman α line profiles currently observed with the *HST* Goddard High Resolution Spectrograph at 20 km s^{-1} resolution reveals that: (1) the typical Doppler width distribution is about the same as that at high redshifts, *i.e.* centered at about 30 km s^{-1} with a small dispersion; and (2) there is very little evidence for structure (*e.g.* an excess of line pairs with separation 50-300 km s^{-1}). So there is a marked contrast between the *transverse* versus *line-of-sight* velocity correlation properties of the absorbers, though it must be noted that the transverse properties result from studies of the relatively strong lines reported here while the line-of-sight properties are deduced from high spectral resolution studies of weaker lines. If these arise from different populations, then the comparison of their properties may be invalid, but, taken at face value, this evidence suggests that we are dealing with coherent structures of low dimensionality, such as sheets or filaments, though the observations could also be explained by flattened disks supported by rotational velocities of (allowing for projection effects) order 200 km s^{-1} but with random velocities which are much smaller than this along each line of sight.

We are in the process of obtaining GHRS observations of this pair of quasars which extend to lower redshifts as well as supporting ground-based observations which may help to resolve some of the questions raised here.

ACKNOWLEDGMENTS. This research was supported by a grant from the Space Telescope Science Institute, AURA Inc., for which we are very grateful. We thank the STScI staff, especially Anne Kinney, Anuradha Koratkar, Tony Keyes, Jennifer Christensen, Howard Bushouse and Krista Rudloff, for their assistance in the data reductions and in helping us to understand the sources of error in the wavelengths. We thank Tom Aldcroft and Jill Bechtold for making their spectral analysis software available to us.

TABLE 1

LYMAN-α ABSORPTION LINES OF QSO PAIR 0107-025A,B WITH $W_0 \geq 0.33$ Å

A No.	λ(Å)	σ_λ	W_0(Å)	σ_{W_0}	z_{abs}	B No.	λ(Å)	σ_λ	W_0(Å)	σ_{W_0}	z_{abs}	A–B Δv(km/s)
			< 0.28			1	1845.17	0.06	0.44	0.04	0.5178	
1	1867.83	0.04	1.74	0.05	0.5364	2	1867.32	0.10	0.66	0.07	0.5360	82 ± 17
2	1894.34	0.10	0.60	0.05	0.5583				< 0.28			
			< 0.22			3	1919.99	0.33	0.38	0.08	0.5794	
3	2016.20	0.16	0.34	0.04	0.6585				< 0.18			
4	2090.33	0.03	0.94	0.03	0.7195	4	2089.55	0.03	0.79	0.03	0.7188	112 ± 4
5	2102.14	0.03	0.72	0.03	0.7292				< 0.16			
6	2172.52	0.03	0.65	0.03	0.7871	5	2173.58	0.07	0.40	0.03	0.7880	−146 ± 7
			< 0.14			6	2200.36	0.03	0.88	0.03	0.8100	
7	2282.03	0.02	0.67	0.02	0.8772	7	2281.61	0.03	0.58	0.02	0.8768	55 ± 5

References

1. Ikeuchi, S., & Ostriker, J.P. *Astrophys. J.*, 301, 522-543 (1986).
2. Bond, J.R., Szalay, A.S., & Silk, J. *Astrophys. J.*, 324, 627-638 (1988).
3. Rees, M.J. *Mon. Not. R. astr. Soc.*, 218, L25-L30 (1986).
4. Lake, G. *Astrophys. J.*, 327, 99-102 (1988).
5. Bahcall, J.N., Bergeron, J., Boksenberg, A., Hartig, G.F., Jannuzi, B.T., Kirhakos, S., Sargent, W.L.W., Savage, B.D., Schneider, D.P., Turnshek, D.A., Weymann, R.J., & Wolfe, A.M. *Astrophys. J. Suppl. Ser.*, 87, 143 (1993).
6. FOS Instrument Team, private communication (1994).
7. McGill, C. *Mon. Not. R. astr. Soc.*, 242, 544-554 (1990).
8. Foltz, C.B., Weymann, R.J., Röser, H-J, & Chaffee, F.H. *Astrophys. J.*, 281, L1-L4 (1984).
9. Smette, A., Surdej, J., Shaver, P.A., Foltz, C.B., Chaffee, F.H., Weymann, R.J., Williams, R.E., & Magain, P. *Astrophys. J.*, 389, 39-62 (1992).
10. Shaver, P.A., & Robertson, J.G. *Astrophys. J.*, 268, L57-L61 (1983).
11. Crotts, A.P.S. *Astrophys. J.*, 336, 550-571 (1989).
12. Shaver, P.A. private communication (1994).
13. Dinshaw, N., Impey, C.D., Foltz, C.B., Weymann, R.J., Chaffee, F.H. *Astrophys. J. Letters*, in press (December 20, 1994).
14. Bechtold, J., Crotts, A.P.S., Duncan, R.C., Fang, Y. *Astrophys. J. Letters*, in press (December 20, 1994).
15. Madau, P. *Astrophys. J. Letters*, 389, L1-L4 (1992).
16. Weymann, R.J., Rauch.M., Williams, R.E., Morris, S.L. and Heap. S. *Astrophys. J.*, 438, in press (January 1995).
17. Lanzetta, K.M., Bowen, D.V., Tytler, D., Webb, J.K. preprint (1994).
18. Morris, S.L., & van den Bergh, S. *Astrophys. J.*, 427, 696-699 (1994).
19. Mo, H.J., & Morris, S.L. *Mon. Not. R. astr. Soc.*, 269, 52-66 (1994).
20. Zaritsky, D. 1994, The Local Group: Comparative and Global Properties, Third ESO/CTIO Workshop, in press.

Figure Captions

FIG. 1:—*HST* FOS spectra of 0107-025A and B as a function of vacuum, heliocentric wavelength. The dotted line in each panel shows the 1-σ errors. Tickmarks indicate significant ($> 5\sigma$) absorption features with rest equivalent widths, $W_o \geq 0.33$ Å. Several strong lines which are not marked can be identified as higher order Lyman lines. The emission feature near 2020 Å is Lyman β+OVI $\lambda\lambda$ 1031, 1037. An exposure of a PtCrNe comparison lamp was obtained immediately following one exposure of each of A and B to minimize the uncertainty in the wavelength calibration due to nonrepeatability in the positioning of the filter-grating wheel which was moved before each target was observed. The spectra were reduced via the STSDAS pipeline processing facility in IRAF using post-COSTAR flat-field and inverse sensitivity files. The bottom panel shows the equivalent width threshold (5σ) for an unresolved line.

FIG. 2:—Probability distribution $P(R)$ normalized to one at its peak as a function of cloud radius for the four coincident and six anticoincident lines observed in the spectra of 0107-025A,B (solid curve). The cumulative probability distribution is also plotted (dashed curve) from which lower and upper limits on the radius of the absorbers can be estimated. A cosmological model with $H_0 = 100\,\mathrm{km\ s^{-1}\,Mpc}$ and $q_0 = 0.5$ was assumed.

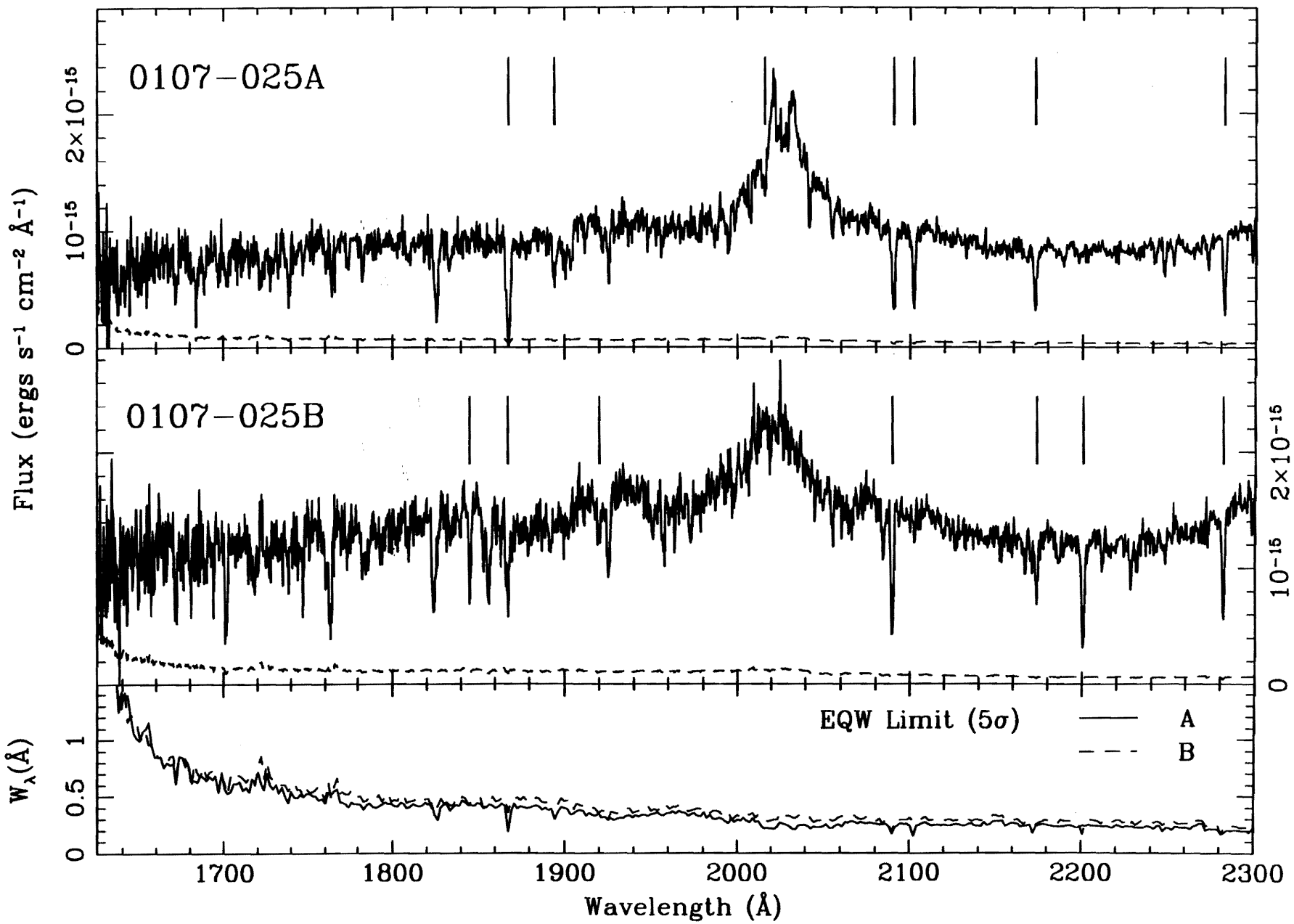
0107−025A
0107−025B
Flux (ergs s^{-1} cm^{-2} Å^{-1})
0
10^{-15}
2×10^{-15}
W_λ(Å)
0
0.5
1
EQW Limit (5σ)
A
B
1700
1800
1900
2000
2100
2200
2300
Wavelength (Å)

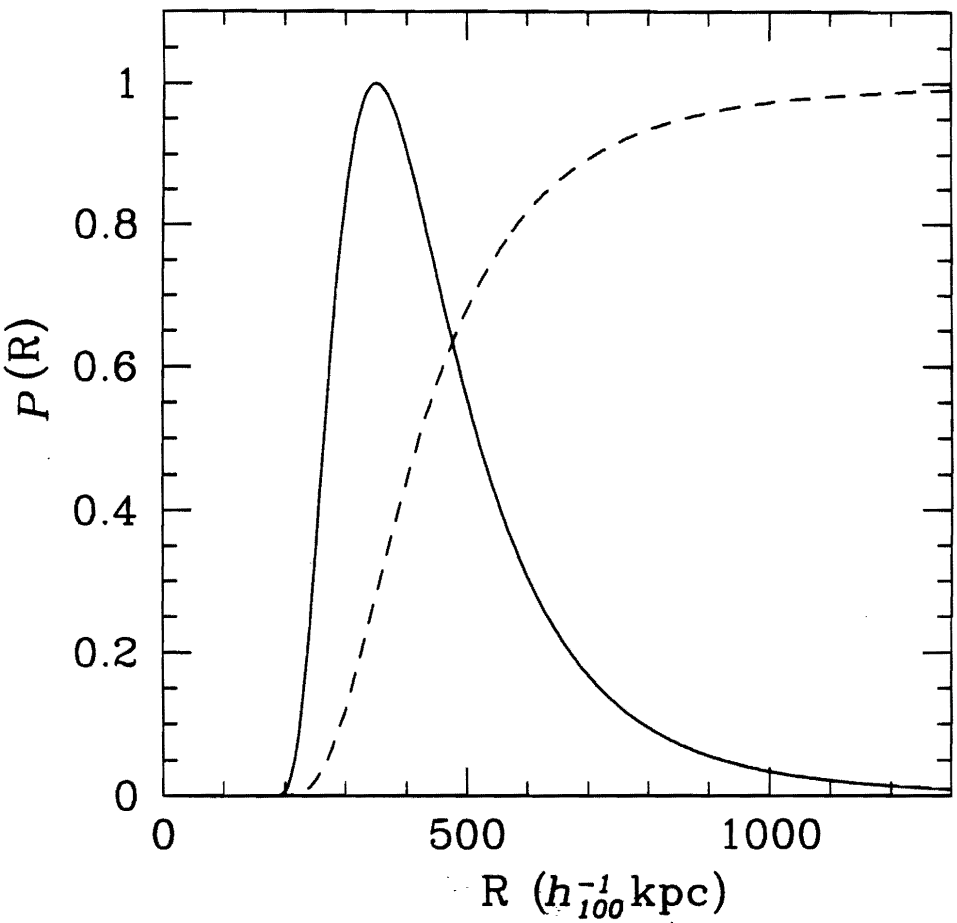
1
0.8
0.6
0.4
0.2
0
P(R)
0
500
1000
R (h_{100}^{-1}kpc)

STEWARD-1246
Fermilab Library
0 1160 0072347 2
FERMILAB
FEB 7 19
LIBRARY

PREPRINTS of the STEWARD OBSERVATORY

THE UNIVERSITY OF ARIZONA
TUCSON, ARIZONA 85721 U.S.A.

No. 1246

MODELING COMPRESSIBLE TURBULENCE WITH MINIMUM FISHER INFORMATION

W. J. Cocke

Steward Observatory
University of Arizona
Tucson, Arizona 85721
email: jcocke@as.arizona.edu

Submitted to Physics of Fluids.

Arizona Theoretical Astrophysics Preprint #94-38

Modeling compressible turbulence with minimum Fisher information

W. J. Cocke
Steward Observatory, University of Arizona, Tucson, AZ 85721
jcocke@as.arizona.edu

The principle of minimum Fisher information is used to work out the joint distribution function of the density and velocity in homogeneous, isotropic, stationary compressible turbulence. It is assumed that the Mach number is low. For an ideal gas in adiabatic motion with $\gamma = 5/3$, the distributions of the density and velocity are nearly Gaussian, but the pressure p has an exponential tail at large values of p. The expression for the pressure-velocity correlation is negative and is proportional to the square of the variance of the density.

I. INTRODUCTION

We apply the principle of minimum Fisher information (MFI) to the problem of understanding the joint distribution function of the density and fluid velocity in adiabatic, compressible turbulent motion. We assume that the turbulence is homogeneous, isotropic, and statistically stationary and that the Mach number is small. We compute the distribution function numerically for the case in which the fluid is an ideal gas with an adiabatic index of 5/3.

The MFI principle has recently been exploited by B. R. Frieden[1,2] as a basis for understanding physical laws. MFI is particularly useful in studying the statistical properties of physical systems. In this paper we consider the density ρ and fluid velocity $\mathbf{u}$ of a turbulent fluid as random variables described by a probability density $P(\rho, \mathbf{w})$, where $\mathbf{w} \equiv \rho\mathbf{u}$ is the mass flux. In this simple version, we consider only the joint probability of these variables at a single point in space and at a given time. Thus we do not attempt to find the correlation between these variables at different locations or at different times.

II. MINIMUM FISHER INFORMATION

The MFI idea may be summarized as follows: Consider a random variable x with probability density $P(x)$. The Fisher information associated with $P(x)$ is defined as

$$I \equiv \int \left(\frac{dP}{dx}\right)^2 \frac{dx}{P}. \tag{1}$$

Minimizing I by varying $P(x)$ leads to physically interesting results if the constraints in the problem are chosen appropriately. One of the constraints is that the average of a kinetic energy be held constant during the variation of $P(x)$. Another constraint often used is normalization, $\int P(x)\,dx = 1$. For example, if the random variable is one of the velocity components v of a molecule in a gas, the constraint $\langle E_{\rm kin}\rangle = \frac{1}{2}m\int v^2 P(v)dv = \frac{1}{2}kT$, together with the normalization constraint, leads to the variational problem

$$\begin{aligned} S &= \int [P'(v)^2/P(v)]dv + \lambda\Big(\int \frac{1}{2}mv^2 P(v)dv - \frac{1}{2}kT\Big) + \mu\Big(\int P(v)dv - 1\Big) \\ &\equiv \int L(P, P')dv = \ \min\,, \end{aligned} \tag{2}$$

where λ and μ are Lagrange multipliers and $P'(v) \equiv dP/dv$.

The Lagrangian for the problem is thus

$$L = \frac{P'^2}{P} + \frac{\lambda}{2} m v^2 P + \mu P \ . \tag{3}$$

The usual Lagrange equation for $P(v)$, $d(\partial L/\partial P')/dv - \partial L/\partial P = 0$, then gives the Boltzmann distribution $P(v) \propto \exp(-av^2)$. One easily finds the Lagrange multipliers to be $\lambda = 8a^2/m$ and $\mu = -4a < 0$, where of course $a = m/2kT$. See Frieden[1] for further details.

In this problem, as well as others, Lagrange's equation is easily linearized by the substitution $P = q^2$. This substitution assures $P \geq 0$.

Frieden[1] showed that the MFI principle (typified by equation (2)) is equivalent to maximizing the mean-square-error of the best possible estimator of the random variable in question.

III. THE TURBULENCE MODEL

We assume that the Fisher information variables are the components of the mass flux $w^\mu \equiv \rho u^\mu$, where we use 4–dimensional relativistic notation, with $\mu = 0, 1, 2, 3$. Here, $u^\mu \equiv dx^\mu/d\tau$ is the 4-velocity of the fluid. This choice of Fisher variables is consistent with formal treatments of Fisher information, in which the preferred variables are components of a conserved 4–vector, such that $\partial w^\mu/\partial x^\mu = 0$. See the comprehensive review by Frieden[2]. In our case this is just the continuity equation, expressing conservation of mass. It must be stated, however, that the choice of Fisher variables is somewhat arbitrary, and there is no guarantee that the components of w^μ are really the appropriate ones. The final justification rests on whether the model gives realistic predictions.

In this paper, we apply the model to the adiabatic motion of a fluid with internal energy density $\epsilon(\rho)$, later specializing to an ideal gas of point particles, for which the energy density of the gas is $p/(\gamma - 1)$, where p is the pressure, and $p = K\rho^\gamma$, with $\gamma = 5/3$.

We could in principle apply our model to relativistic turbulence, but this would be very difficult, so we content ourselves with the Newtonian, nonrelativistic case. In the nonrelativistic limit, then, we have $w^\mu \approx \rho(1, \mathbf{u})$, where $\mathbf{u}$ is the Newtonian fluid velocity. The Fisher variables become just ρ and $\mathbf{w}$. We use three constraints in the MFI principle; namely, we use the mean values of the fluid kinetic energy density and the internal energy density, and (as in Sec. II) normalization. These constraints are allowed for by three Lagrange multipliers λ_1, λ_2, and λ_3. The fluid kinetic energy density is $\rho \mathbf{u}^2/2 = \mathbf{w}^2/2\rho$.

The variables ρ and $\mathbf{w}$ have different dimensions, and we must introduce a scale factor c having dimensions meters/sec into the MFI Lagrangian, which we write in a way similar to equation (3) as

$$L = \frac{1}{P} \nabla_w P \cdot \nabla_w P + \frac{1}{c^2 P} \left(\frac{\partial P}{\partial \rho}\right)^2 - \left(\frac{\lambda_1 \mathbf{w}^2}{2\rho} + \lambda_2 \epsilon + \lambda_3\right) P \quad . \tag{4}$$

Using the substitution $P = q^2$ leads to the Lagrange equation

$$\nabla_w^2 q + \frac{1}{c^2} \frac{\partial^2 q}{\partial \rho^2} = \left(\frac{\lambda_1}{2\rho} w^2 + \lambda_2 \epsilon(\rho) + \lambda_3\right) q \quad , \tag{5}$$

where ∇_w^2 is the Laplacian in 3–dimensional w–space and $w^2 \equiv \mathbf{w}^2$.

We wish to solve this equation for $P = q^2(\rho, \mathbf{w})$ under the boundary conditions that P be integrable and that $q(0, \mathbf{w}) = 0$. In general this is a very difficult problem, even numerically, but we can find an approximate solution for low Mach number, where $u^2 << d\epsilon/d\rho = v_s^2$, v_s being the sound speed.

In this case one may use the *Ansatz* $q = \psi(\rho) \exp[-a(\rho) w^2]$ for the low-Mach-number limit. Substituting this expression into equation (5) and neglecting the term in w^4 yields the equation

$$\begin{aligned} \nabla_w^2 q + \frac{1}{c^2} \frac{\partial^2 q}{\partial \rho^2} &\approx e^{-aw^2} \left\{ \left[(4a^2 - c^{-2} a'') \psi - 2c^{-2} a' \psi' \right] w^2 + c^{-2} \psi'' - 6a\psi \right\} \\ &\approx e^{-aw^2} \left(\frac{\lambda_1}{2\rho} w^2 + \lambda_2 \epsilon(\rho) + \lambda_3 \right) \psi \quad . \end{aligned} \tag{6}$$

Here, the prime indicates differentiation with respect to ρ. To interpret a, note that the probability density for w at fixed ρ is, by Bayes' theorem,

$$P(\mathrm{w}|\rho) = \frac{P(\mathrm{w},\rho)}{P(\rho)} = \left(\frac{2a}{\pi}\right)^{3/2} e^{-2aw^2} \quad , \tag{7}$$

since $P(\rho) = \psi(\rho)^2 \int d^3w \exp[-2a(\rho)w^2]$. Note that the *Ansatz* automatically involves a Gaussian distribution for the velocity, for low Mach number.

Taking into account the 3–dimensional nature of the integral over w–space, we may easily use equation (7) to evaluate the expectation of w^2 for fixed ρ, which we denote by $E[w^2|\rho]$. The result is

$$E[w^2|\rho] = \frac{3}{4a(\rho)} \quad . \tag{8}$$

We now show that one may neglect the term in a'' in equation (6), assuming that a'' is of order $a\rho^{-2}$ and that c is equal to or greater than the sound speed v_s. From these assumptions it follows directly that $|a''|c^{-2} \lesssim a(\rho v_s)^{-2}$. Also note that a itself, by virtue of equation (8), is of order $a \approx E[w^2]^{-1} \approx E[(\rho u)^{-2}]$. The neighboring term $4a^2$ is then of order $4a^2 \approx a(\rho u)^{-2}$. But in the limit of low Mach number, $u << v_s$, and therefore $|a''|c^{-2} << 4a^2$. It is not consistent to make the same argument about the term in ψ''.

Since equation (6) must hold for all w, it breaks up into the two equations $4a^2\psi - 2c^{-2}a'\psi' \approx \lambda_1\psi/(2\rho)$ and $c^{-2}\psi'' - 6a\psi \approx (\lambda_2\epsilon + \lambda_3)\psi$.

For integrating these equations numerically it is convenient to introduce the new variable $Z \equiv \psi'/\psi$. The above equations then become

$$2a'Z \approx c^2\left(4a^2 - \frac{\lambda_1}{2\rho}\right) \tag{9}$$

$$Z' + Z^2 \approx c^2\left(6a + \lambda_2\epsilon + \lambda_3\right) \quad . \tag{10}$$

An approximate solution of equation (10) may be obtained in the limit of large c by noting that as $c \to \infty$, $Z = O(c)$. The term Z' in equation (10) may then be neglected. We show in the next section that this is actually the same as the low-Mach-number limit, at least for the ideal gas of point particles. In this approximation we get

$$Z \approx \pm c\sqrt{6a + \lambda_2\epsilon + \lambda_3} \quad . \tag{11}$$

This relation is actually the lowest-order equation in a WKB approximation and is not valid near or between the "classical turning points," where $Z \approx 0$. We discuss this further in the next section, where we apply the formalism to an ideal gas of point particles.

It is well known that the velocity components in atmospheric turbulence are approximately normally distributed, but that there are more zeros and more strong gusts than would be the case for an exact Gaussian[3]. The approximation of low Mach number used in this paper is responsible for the exactly normal distribution obtained here. It may be that relaxing this condition would produce a more realistic model.

IV. APPLICATION TO AN IDEAL GAS OF POINT PARTICLES

We now integrate equation (10) numerically, using the approximation $a(\rho) \approx \sqrt{\lambda_1/8\rho}$. Equation (8) shows that this approximation implies $E[U^2|\rho] = E[w^2|\rho]/\rho^2 \propto \rho^{-3/2}$, so that the velocity dispersion gets larger as ρ decreases.

We show below that this approximation for $a(\rho)$ is valid over a wide range of ρ and is consistent with the assumption that the Mach number is small, at least for the parameter values used in this section, which we now discuss.

We first show how to fix λ_1: Let the turbulence be characterized by the rms turbulent velocity U_0 and the density ρ_0 at which $P(\rho,0) = \psi(\rho)^2$ is a maximum. Let $w_0 \equiv \rho_0 U_0$. Then by equation (8) $w_0^2 = E[w^2|\rho_0] = 3/4a(\rho_0)$. So if $a(\rho) \approx \sqrt{\lambda_1/8\rho}$, we have

$$\lambda_1 \approx 8\rho_0 a(\rho_0)^2 = \frac{9}{2\rho_0^3 U_0^4} \quad . \tag{12}$$

The multiplier λ_2 may be fixed by recognizing that equation (10) is like the Schrödinger wave equation for a particle in a potential $V(x) \propto 6a(x) + \lambda_2\epsilon(x)$. (Recall that $Z' + Z^2 = \psi''/\psi$.)

For an ideal gas of point particles, $\gamma = 5/3$, and the energy density is $\epsilon = 3p/2$. For adiabatic motion $p(\rho) = K\rho^{5/3}$. Thus the maximum value of ψ (i. e., $\psi(\rho_0)$) occurs where the "potential" $V(\rho) = 6a + 3\lambda_2 K\rho^{5/3}/2 \approx 3\sqrt{\lambda_1/2\rho} + 3\lambda_2 K\rho^{5/3}/2$ is a minimum. Knowing λ_1 from equation (12), one can then find λ_2 by taking $dV/d\rho = 0$ at ρ_0, getting

$$\lambda_2 \approx \frac{9}{10K} U_0^{-2}\rho_0^{-11/3} \quad . \tag{13}$$

The multiplier λ_3 then follows as an eigenvalue of equation (10), under the boundary conditions that $Z(\rho) \to +\infty$ as $\rho \to 0$ and $Z(\rho) \to -\infty$ as $\rho \to +\infty$. However, one may get an estimate of λ_3 by using equations (11), (12), and (13) and assuming that $Z(\rho_0) \approx 0$. The result is

$$\lambda_3 \approx \frac{117}{20} U_0^{-2}\rho_0^{-2} \quad . \tag{14}$$

The parameter c may be found by noting that the variance $\delta\rho$ of ρ near ρ_0 is given by $P(\rho,0) \approx \exp[2\int_{\rho_0}^{\rho} Z(\rho')d\rho'] \approx \exp[-(\rho-\rho_0)^2/2\delta\rho^2]$. It then follows that $2Z' \approx 1/\delta\rho^2 \approx \pm c(V+\lambda_3)^{-1/2}V'$. Note that $V(\rho_0) + \lambda_3 \approx 0$ and $V'(\rho_0) \approx 0$. Therefore, $V(\rho) \approx \frac{1}{2}V''(\rho_0)(\rho-\rho_0)^2$. One may combine these relations with equations (11) - (14) to find

$$c \approx \frac{U_0\rho_0^2}{\delta\rho^2}\sqrt{\frac{4}{39}} \quad . \tag{15}$$

As an application of this technique, we have computed an approximate solution of equation (10) for our point-particle gas at a characteristic pressure of 1 atm $\approx 10^5$ Nt/m^2 and a characteristic density of $\rho_0 = 1$ kg/m^3, corresponding to standard temperature and pressure at sea level. This gives $K = 10^5$ in MKS units. We assume an rms turbulent velocity of $U_0 = 5.2$ m/sec. Equations (12) and (13) then yield $\lambda_1 = 0.006173$ and $\lambda_2 = 3.333 \times 10^{-7}$. We have fixed the width of $\psi(\rho)$ by setting $c = 3 \times 10^4$ m/sec in equation (15), getting $\delta\rho = 0.0075$ kg/m^3 .

The WKB approximation was used for the actual computation of $Z(\rho)$, with our large parameter c playing the role of the quantum-mechanical $\sqrt{2m}/\hbar$. See, for example, the book by Schiff[4], who gives details on fitting Bessel functions together at the classical turning points. In the quantum mechanical case, the assumption of large quantum number is generally used to allow cosine solutions in the region between the turning points. In this case, however, we are interested in a solution with a single maximum, so we must use the Bessel functions $J_{\pm 1/3}$ themselves for the fitting. If the turning points are ρ_1 and ρ_2, we define

$$\xi(\rho) \equiv c\int_{\rho_1}^{\rho} \sqrt{-V(\rho)-\lambda_3}\,d\rho \quad , \quad \rho > \rho_1$$
$$\bar{\xi}(\rho) \equiv c\int_{\rho}^{\rho_2} \sqrt{-V(\rho)-\lambda_3}\,d\rho \quad , \quad \rho < \rho_2 .$$

The fit was then obtained by adjusting λ_3, ρ_1, and ρ_2 so that the functions $\sqrt{\xi}[J_{1/3}(\xi) + J_{-1/3}(\xi)]$ and $\sqrt{\bar{\xi}}[J_{1/3}(\bar{\xi}) + J_{-1/3}(\bar{\xi})]$ met at their maxima, assuring that ψ and its derivative were continuous everywhere. For the parameter values given in the paragraph just below equation (15), the fit gives $\rho_1 \approx 0.988875$, $\rho_2 \approx 1.011202$, and $\lambda_3 \approx -0.2163574$. This value of λ_3 compares well with the estimate given by equation (14), which is -0.216346.

Figure 1 is the resulting graph of the quantity $Z \equiv \psi'/\psi$. The abscissa is the mass density ρ in kg/m^3. Correspondingly, Z (the logarithmic slope of ψ) crosses zero at $\rho_0 = 1$ kg/m^3. This means that the density distribution is roughly a Gaussian with a peak at ρ_0. The variance of the Gaussian is small, about 0.0075 kg/m^3 as stated above. The sound speed is $v_s = 300$ m/sec, giving a Mach number of about 0.017.

A general feature of this model is that the parameter c is arbitrary and was used in equation (15) to set the width of the density distribution. With c fixed, however, the model is completely determined, and one can go on to predict such quantities as the correlation between pressure and velocity. We do this in the next section.

Generally, the variance of the density distribution is given approximately by $\delta\rho \approx \rho_0 M^2$, M being the Mach number. So the variance appropriate to $M = 0.017$ is about 3×10^{-4} kg m^{-3}, or a factor of thirty smaller than that given by Figure 1. But one can use equation (15) to show that one could reach this value of $\delta\rho$ by going to $c = 2 \times 10^7$ m/sec. The numerical integrations become difficult for such a large value of c.

We have mentioned that the term Z' in equation (10) is generally much smaller than any of the others, so that one obtains equation (11). This equation breaks down at $Z \approx 0$, since its right-hand side actually vanishes at the turning points ρ_1 and ρ_2, rather than at ρ_0. Elsewhere, however, for the parameter values leading to Figure 1, equation (11) represents Z to better than 1% accuracy over the range of the figure. Therefore the shape of the curve in Figure 1 is the same for all values of c for which the Mach number is low; we need only change the scale of the ordinate by a factor of c to find Z for any such value of c. This means $\delta\rho << \rho_0$, or, from equation (15), $c >> U_0$.

We can now discuss the approximation $a(\rho) \approx \sqrt{\lambda_1/8\rho}$, which results from neglecting the term in $a'Z$ in equation (9). If this approximation holds, equation (12) implies $a(\rho) \approx 3/(4U_0^2\rho_0^{3/2}\rho^{1/2})$, so that a typical value for a' is $a' \approx -3/(8U_0^2\rho_0^3) \approx -0.014$. From Figure 1, a typical value for $|Z|$ is 5×10^3, and so the left-hand side of equation (9) is, numerically, about 140 kg^{-4} m^{10} sec^2. But the first term on the right-hand side is $4c^2a^2 \approx 9c^2/(4U_0^4\rho_0^4) \approx 2.8 \times 10^6$ in the same units. Therefore the left-hand side of (9) is much less than the individual terms on the right-hand side and may be neglected. Since $a' \propto \rho^{-3/2}$ and $a^2 \propto \rho^{-1}$, the approximation breaks down for very small ρ.

For very large ρ, the expression (11) may be used to show that $a'Z \propto \rho^{-2/3}$, whereas $a^2 \propto \rho^{-1}$. Thus there are troubles at very large ρ, as well. But for the range covered by experiments and simulations (perhaps $0.5 \lesssim \rho \lesssim 2.0$), the approximation should be valid. One can easily show that the approximation gets even better as c is increased, for fixed U_0 and ρ_0.

Similar arguments may be advanced for neglecting $c^{-2}a''$ as compared with $4a^2$ in equation (6). We have $a'' \approx 9/(16U_0^2\rho_0^{3/2}\rho^{5/2})$, and so a typical value for $c^{-2}a''$ is $9/(16c^2U_0^2\rho_0^4) \approx 2.3 \times 10^{-11}$, whereas $4a^2 \approx 3.1 \times 10^{-3}$.

Figure 1 shows that $Z(\rho)$ is very nearly a straight line near the central value $\rho_0 \approx 1$, so the distribution of the density at fixed $\mathbf{w} = 0$ is roughly Gaussian. The MFI principle thus predicts that experiments and direct numerical simulations should show small deviations of $P(\rho, 0)$ from an exact Gaussian.

The marginalized pressure distribution $P(p)$ is also interesting. A plot of $\log_{10}[P(p)]$ is shown in Figure 2, where we see that the distribution becomes approximately exponential for large values of p. We comment on this further in Section VI.

V. MEAN VALUES AND THE CORRELATION BETWEEN DENSITY AND VELOCITY

In this section we evaluate various expectation values assuming that $a(\rho) \approx \sqrt{\lambda_1/8\rho}$ and that one can fit Z with a quadratic as $Z(\rho) \approx -(\rho - \rho_0)/2\delta\rho^2 + \frac{3}{2}\beta(\rho - \rho_0)^2$, where we also assume $|\beta\delta\rho^3| << 1$. This fit need apply only over an interval that is several times the variance $\delta\rho$. For Figure 1, these conditions are satisfied, since we have $\beta \approx 2000$ (kg/m^3)$^{-3}$and $\delta\rho \approx 0.0075$ kg/m^3.

First we investigate the normalization $\int\int \psi^2 e^{-2aw^2} d^3w d\rho = 1$, with $\psi(\rho) =$
$A_0 \exp[\int_{\rho_0}^{\rho} Z(\rho')d\rho']$, A_0 being a constant. Changing variables to $r = \rho - \rho_0$ gives $\psi(r)^2 = A_0^2 \exp[2\int_0^r Z(r')dr'] \approx$

$\exp[-r^2/2\delta\rho^2 + \beta r^3]$. Integrating over w yields

$$\int\int \psi^2 e^{-2aw^2} d^3w\, d\rho \approx A_0^2 \int_{-r_c}^{r_c} e^{-r^2/2\delta\rho^2} e^{\beta r^3} \left(\frac{\pi}{a}\right)^{3/2} dr \approx 1 \quad , \tag{16}$$

where $r_c^2 >> 2\delta\rho^2$ is a suitable cutoff such that $\beta r_c^3 << 1$. For the example in Figure 1, $r_c \approx 0.04$ kg m^{-3} would suffice.

We can then expand $e^{\beta r^3} \approx 1 + \beta r^3 + (\beta r^3)^2/2$ and $a(r)^{-3/2} \approx (8\rho_0/\lambda_1)^{3/4}(1 + 3r/4\rho_0 - 3r^2/32\rho_0^2)$. One may then extend the integration in equation (16) to $\pm\infty$ and obtain to third order in $\delta\rho/\rho_0$ and $\beta\delta\rho^3$

$$A_0^{-2} \approx \frac{\pi^2}{2}\left(\frac{8\rho_0}{\lambda_1}\right)^{3/4} \delta\rho\left[1 - \frac{3}{32}\frac{\delta\rho^2}{\rho_0^2} + \frac{9}{4}\beta\delta\rho^3\frac{\delta\rho}{\rho_0} + \frac{15}{2}(\beta\delta\rho^3)^2\right] \quad .$$

Similarly, one can show that to the same order of smallness the mean value of ρ, abbreviated $\langle\rho\rangle$, is

$$\langle\rho\rangle \approx \rho_0\left(1 + \frac{3}{4}\frac{\delta\rho^2}{\rho_0^2} + 3\beta\delta\rho^3\frac{\delta\rho}{\rho_0}\right) \quad .$$

Likewise, from equation (8),

$$\langle U^2\rangle = \left\langle\frac{w^2}{\rho^2}\right\rangle \approx U_0^2\left(1 + \frac{3}{4}\frac{\delta\rho^2}{\rho_0^2} - \frac{9}{2}\beta\delta\rho^3\frac{\delta\rho}{\rho_0}\right)$$
$$\langle\rho U^2\rangle \approx \rho_0 U_0^2\left(1 - \frac{3}{2}\beta\delta\rho^3\frac{\delta\rho}{\rho_0}\right)$$

The density–velocity correlation then becomes

$$\begin{aligned} E[(\rho - \langle\rho\rangle)U^2] &\approx -\frac{3}{2}\langle U^2\rangle\frac{\delta\rho^2}{\rho_0} \\ &\approx -\frac{3}{2}U_0^2\frac{\delta\rho^2}{\rho_0} \quad . \end{aligned} \tag{17}$$

Note that the terms in β have cancelled and that the expression does not depend on the equation of state.

If $p = K\rho^\gamma$, we can easily convert this into the pressure–velocity correlation as

$$E[(p - \langle p\rangle)U^2] \approx -\frac{3}{2}\gamma U_0^2\langle p\rangle\frac{\delta\rho^2}{\rho_0^2} \quad . \tag{18}$$

The sign of this correlation is in agreement with the Millionshchikov hypothesis[5].

VI. SUMMARY AND CONCLUSIONS

We have demonstrated that the MFI principle can predict the distribution of density and pressure in homogeneous, isotropic, compressible, stationary turbulence. At low Mach number, for an ideal gas of point particles in adiabatic motion ($\gamma = 5/3$), these distributions are nearly Gaussian, although the pressure distribution shows an exponential tail at large p.

For incompressible turbulence, various investigations show exponential tails for certain distributions. See for example Lane et al[6], who find exponential tails for the temperature distribution in experiments with passive transport in incompressible turbulence. The exponential character seems, however, to be due to eddy transport of large temperature differences from distant locations.

Holzer and Siggia[7] show exponential distributions in numerical experiments with Gaussian velocity distributions, and Pumir[8] has demonstrated that direct numerical simulations can yield pressure distributions

which are exponential for $p < \bar{p}$ and Gaussian for $p > \bar{p}$. Both of these papers, however, treat incompressible turbulence, whereas the results of the present paper are for the compressible case.

For incompressible turbulence, the density cannot be used as a Fisher variable since it is constant. Thus the compressible and incompressible cases would seem to be quite different from each other from the point of view of MFI.

For an ideal point-particle gas, we predict a negative pressure-velocity correlation which depends on γ, as given by equation (18).

ACKNOWLEDGMENTS

We thank Bruce J. Bayly, B. Roy Frieden, and R. H. Kraichnan for their help and encouragement.

References

[1]B. R. Frieden, "Fisher information, disorder, and the equilibrium distribution of physics," Phys. Rev. A **41**, 4265 (1990).

[2]B. R. Frieden, "Physical Information and the Derivation of Electron Physics," Advances in Imaging and Electron Physics **90**, 123 (1994).

[3]J. A. Dutton and D. G. Deaven, "Some observed properties of atmospheric turbulence," in *Statistical Models and Turbulence, Lecture Notes in Physics 12* (Springer-Verlag, Berlin, 1971), pp. 352 - 383.

[4]L. I. Schiff, *Quantum Mechanics* (McGraw-Hill, New York, 1955), pg. 187.

[5]A. S. Monin and A. M. Yaglom, *Statistical Fluid Mechanics: Mechanics of Turbulence* (MIT Press, Cambridge, 1975), Vol. 2, pg. 251.

[6]B. R. Lane, O. N. Mesquita, S. R. Meyers, and J. P. Gollub, "Probability distributions and thermal transport in a turbulent grid flow," Phys. Fluids A **5**, 2255 (1993).

[7]M. Holzer, and E. Siggia, "Skewed, exponential pressure distributions from Gaussian velocities," Phys. Fluids A **5**, 2525 (1993).

[8]A. Pumir, "A numerical study of pressure fluctuations in 3-d incompressible, homogeneous isotropic turbulence," Phys. Fluids **6**, 2071 (1994).

Figure Captions

Figure 1. $Z(\rho)$, the logarithmic derivative of $\psi(\rho)$ for an ideal gas of point particles, with $\rho_0 = 1$ kg/m^3, $U_0 = 5.2$ m/sec, and a variance $\delta\rho = 0.0075$ kg/m^3. The nearly linear appearance shows that $\psi(\rho)$ is approximately Gaussian.

Figure 2. $\log_{10}[P(p)]$, the logarithm of the pressure distribution function for an ideal gas of point particles for the same parameters as in Figure 1. The abscissa is the pressure scaled by $p_0 = 1$ atm $= 1 \times 10^5$ Nt/m^2.

Cocke - Figure 1

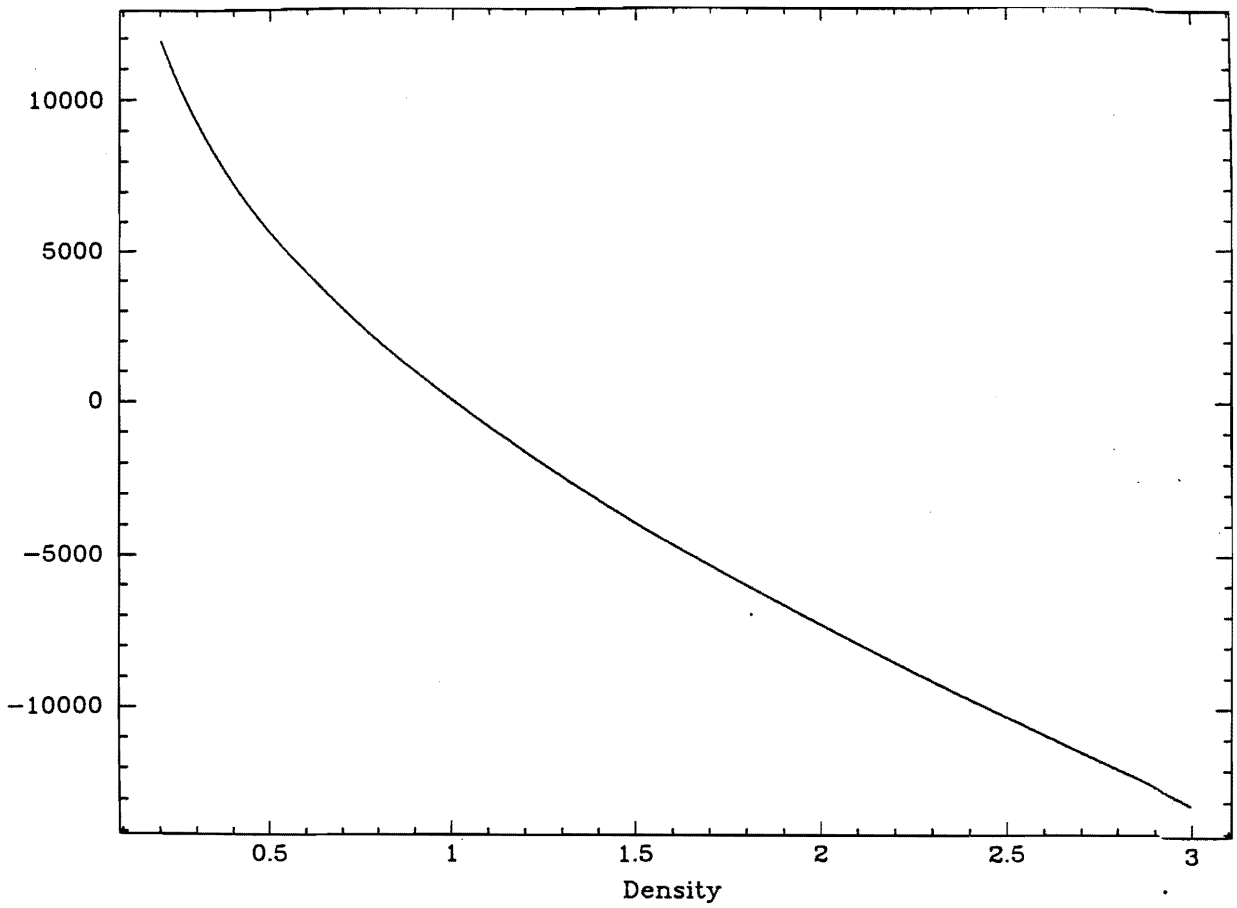
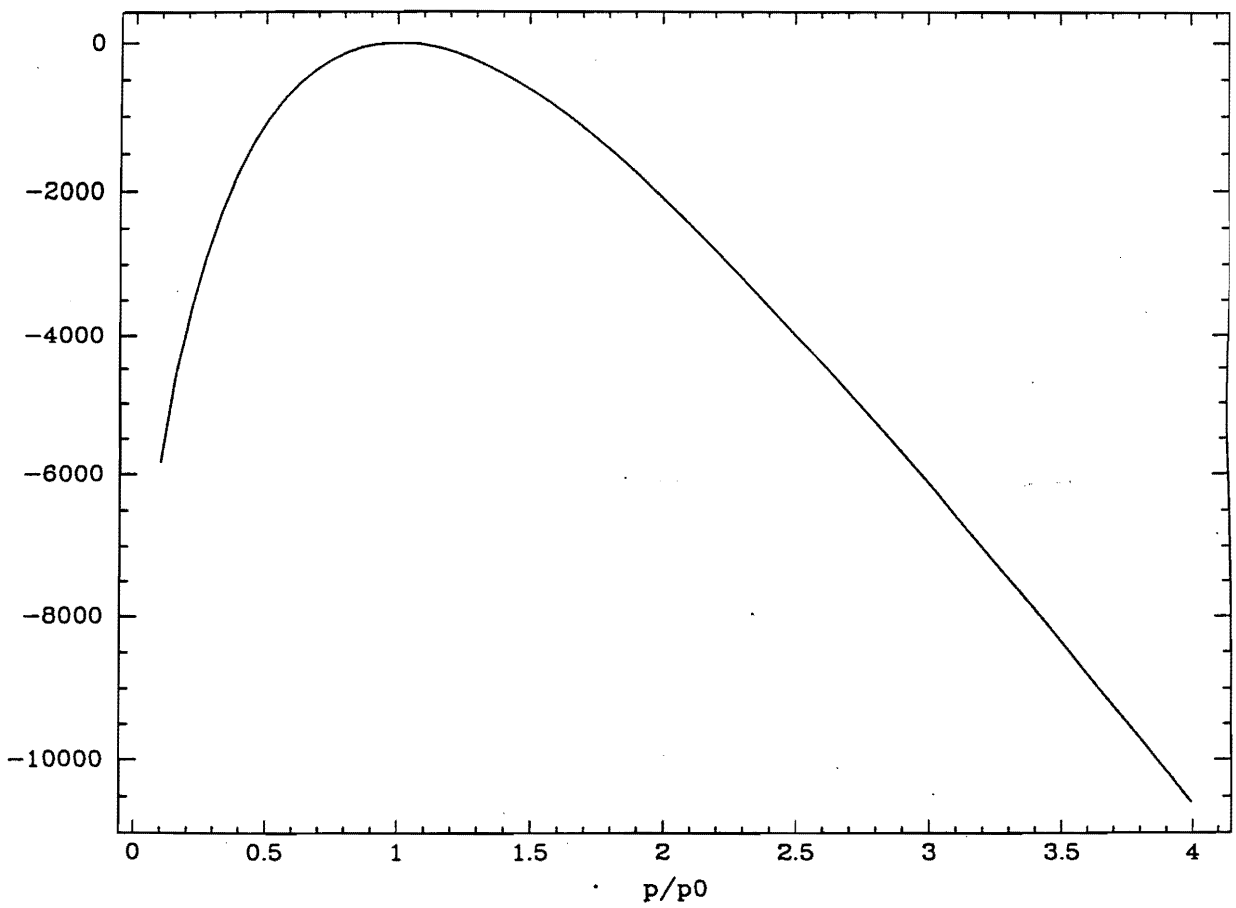
Cocke - Figure 2